Wavefront Amplitude Variation of TPF's High Contrast Imaging Testbed: Modeling and Experiment

Fang Shi*, Andrew E. Lowman, Dwight C. Moody, Albert F. Niessner, and John T. Trauger

Jet Propulsion Laboratory, California Institute of Technology, Pasadena, CA 91109

ABSTRACT

Knowledge of wavefront amplitude is as important as the knowledge of phase for a coronagraphic high contrast imaging system. Efforts have been made to understand various contributions of the amplitude variation in Terrestrial Planet Finder's (TPF) High Contrast Imaging Testbed (HCIT). Modeling of HCIT with as-built mirror surfaces has shown an amplitude variation of 1.3% due to the phase-amplitude mixing for the testbed's front-end optics. Experimental measurements on the testbed have shown the amplitude variation is about 2.5% with the testbed's illumination pattern has a major contribution as the low order amplitude variation.

Keywords: TPF, coronagraph, high contrast imaging, wavefront sensing and control

1. INTRODUCTION

The mission of Terrestrial Planet Finder (TPF) will detect and characterize earth-like planet around nearby stars [1]. TPF Coronagraph mission uses a high contrast coronagraphic imaging system to suppress the stellar light from star. The small angular separation of star and planets (50 – 200 milli-arcsecond) requires image contrast of 10^{-10} within a few λ/D of the main star in visible bandwidth.

The high contrast requirements present a challenge to TPS's wavefront sensing and control. In most convention active/adaptive optics (AO) systems the wavefront sensing and control is done to sense and compensate wavefront phase error only. The assumption is that with star at infinity and a system with a uniform optics coating will present uniform wavefront amplitude. For a normal diffraction limited imaging system ($\lambda/20$) this assumption is adequate. However, this assumption no longer holds for the high contrast imaging system with phase error smaller than $\lambda/1000$. At this level the wavefront amplitude variation from the perfect uniformity, or amplitude error, plays a significant role in reducing the image contrast. The wavefront of an imaging system at the exit pupil can be expressed as a complex function $E(x,y)$,

$$E(x,y) = A(x,y)\exp(-ik\phi(x,y))$$

where $A(x,y)$ is the wavefront amplitude and $\phi(x,y)$ the wavefront phase error. For a perfect imaging system the wavefront amplitude is constant ($A(x,y) = A_0$) across the pupil and has no phase error ($\phi(x,y)=0$). For a system with small amplitude error (δ) and phase error (ϕ) the complex wavefront may be approximated with,

$$E(x,y) \approx A_0(1+\delta)\cdot(1-ik\phi) \approx A_0(1+\delta-ik\phi)$$

where the higher order terms are dropped. The scatter light from the amplitude and phase errors will have the form of [2],

* Fang.Shi@jpl.nasa.gov; Phone: 818-393-5236

$$\frac{I}{I_0} \approx \frac{|FT(\delta)|^2}{A_0^{\,2}} + \frac{|FT(k\phi)|^2}{A_0^{\,2}}$$

where $I_0 = A_0^2$ is the ideal image intensity, operator FT stands for Fourier transform, and again we dropped the high order cross terms. In other words, the amplitude error will affect the image contrast in a similar way as that of phase error; both create speckles in the image field. To the first order, the strength of amplitude error of $\delta = 1\%$ variation from uniformity is equivalent to a phase error of $\phi = \lambda/628$. For TPF it is critical to consider the amplitude error in the system wavefront sensing and control in addition to the phase error. Currently two deformable mirrors (DM) in a Michelson interferometer configuration provides TPF with both phase and amplitude controllability.

There are many sources which will contribute a wavefront amplitude error. Besides the non-uniformity of the optical coatings and non-uniform transmittance of optical materials in the system the amplitude error can also arise from the "phase-amplitude mixing" in which a wavefront phase error, such as mirror surface error from an optics that is located away from the pupil, mixes into the amplitude error at exit pupil after the phase aberrated wavefront has propagated the distance between the optics and exit pupil. This part of amplitude error will exist even for a system with a perfect coating. For an optical testbed in the laboratory, such as TPF's High Contrast Imaging Testbed (HCIT), the illumination pattern of the artificial stellar source will also cause amplitude drooping, a low order form of amplitude error. Also for a real system other effects such as interference of ghost image from the transmissive optics and dust scatter will also present as a wavefront amplitude error.

This paper summarizes our current efforts to understand the amplitude error existing in HCIT. Our efforts include both modeling and experiment on HCIT. In our modeling study a surface-to-surface diffraction propagation optical model of HCIT was used to study the phase-amplitude mixing from the surface error of optics. In our experimental study various experiments are carried out on HCIT to accurately measure the amplitude error. The paper is organized as follows. In Section 2 we describe the TPF's High Contrast Imaging Testbed. In Section 3 we discuss modeling study and followed by Section 4 in which we describe our experimental study and present the results for the HCIT amplitude error measurement. Finally we summarize our current work and outline our future work in Sections 5.

2. HCIT DESCRIPTION

High Contrast Imaging Testbed (HCIT) is built to develop and demonstrate coronagraphy technology for TPF. Figure 1 shows the layout of the HCIT. The optics sits on a 5x7 foot optical table. It resides in a thermally controlled vacuum tank which provides the desirable environment with vibration isolation, atmospheric turbulence free vacuum and sub-Kelvin thermal stability. An artificial star is simulated by a five micron pinhole illuminated by an optical fiber. Various light sources can be fed into the other end of fiber which provide the testbed with a light source of bandwidth from narrow (laser) to broadband ($\Delta\lambda/\lambda_0 = 20\%$ or more). The light is collimated by an off-axis parabolic mirror (OAP #1) to a high-density deformable mirror (DM), which performs the wavefront control. The aperture mask on the DM defines the system pupil of the HCIT. After the DM, the light is focused by OAP #2 to an occulting mask which attenuates the star light; if a planet source were present, it would be minimally affected. The transmitted light is collimated by OAP #3 and propagates to Lyot plane which is conjugated to the DM. The pupil at Lyot is the same size as DM. A Lyot stop will block the ring-like residual light formed from diffraction around the occulting mask while letting most of the planet light through. The remaining stellar and planet light is then focused by OAP #4 and magnified ($M \approx 3$) by the last pair of OAPs (OAP #5 and #6) for a proper sampling on the CCD science camera. The "front-end optics", from artificial star to occulting mask, works with wavefront sensing and control algorithm to provide the stellar light suppression, so its wavefront is most interesting for the testbed. The "back-end optics", from the occulting mask to the science camera, supports experiment with phase diverse wavefront sensing and shaped pupil experiment [3, 4, 5]. Original designed for wavefront sensing and control with phase retrieval the testbed can also form a image of pupil on science camera with a flip-in pupil lens. The mirrors in the testbed are commercial off-the-shelf $\lambda/20$ optics. Each mirror has been measured with Zygo interferometer in their mounted state.

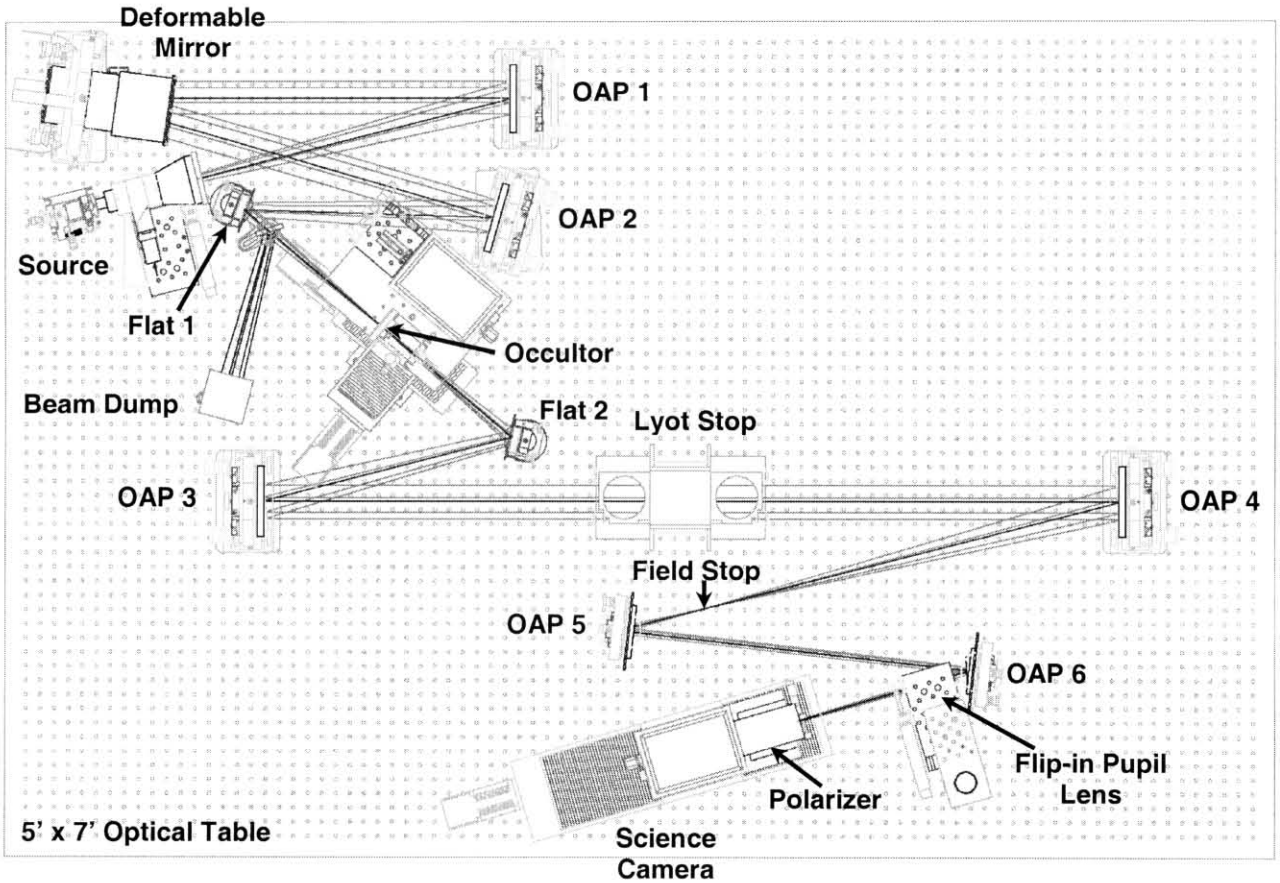

Figure 1. High Contrast Imaging Testbed layout. The drawing is from the testbed's CAD model.

3. MODELING STUDY OF HCIT AMPLITUDE ERROR

Using the HCIT "as-built" prescriptions a realistic optical model has been setup in MACOS, a versatile optical modeling tool developed by JPL which has been used for many flight projects [6]. To study the effect of phase-amplitude mixing a full surface-to-surface near-field diffraction propagation is used for the front-end optics. The mirror surface errors can be added into each mirror in the model. After the diffraction propagation the complex wavefront ($E = A\ exp(-ik\phi)$) is examined at the exit pupil and compared with ideal (no mirror surface error) case ($E_0 = A_0\ exp(-ik\phi_0)$). The amplitude error δ is calculated as,

$$\delta = \frac{\left\| E \right| - \left| E_0 \right\|}{\left| E_0 \right|} = \frac{\left| A - A_0 \right|}{A_0}$$

All HCIT mirrors have been carefully measured and characterized using a Zygo interferometer before they were put into the testbed. To best represent the mirror in the testbed the mirrors were measured in their optical mount with the orientation registered so the measurement can be readily put into the optical model. Figure 2 shows the modeling results of amplitude errors caused by HCIT mirror surface errors. In the figure the three columns on the shows amplitude error caused by phase error of each individual mirror and the last column shows the combined amplitude error of all three mirrors of the front-end optics. The X and Y cross-section of the amplitude error are also plotted in addition to the amplitude error map for more detailed view. Absent from the figure is the amplitude error contribution from the DM mirror surface error. Because DM, by design and confirmed by MACOS model, is at the pupil so its surface error will

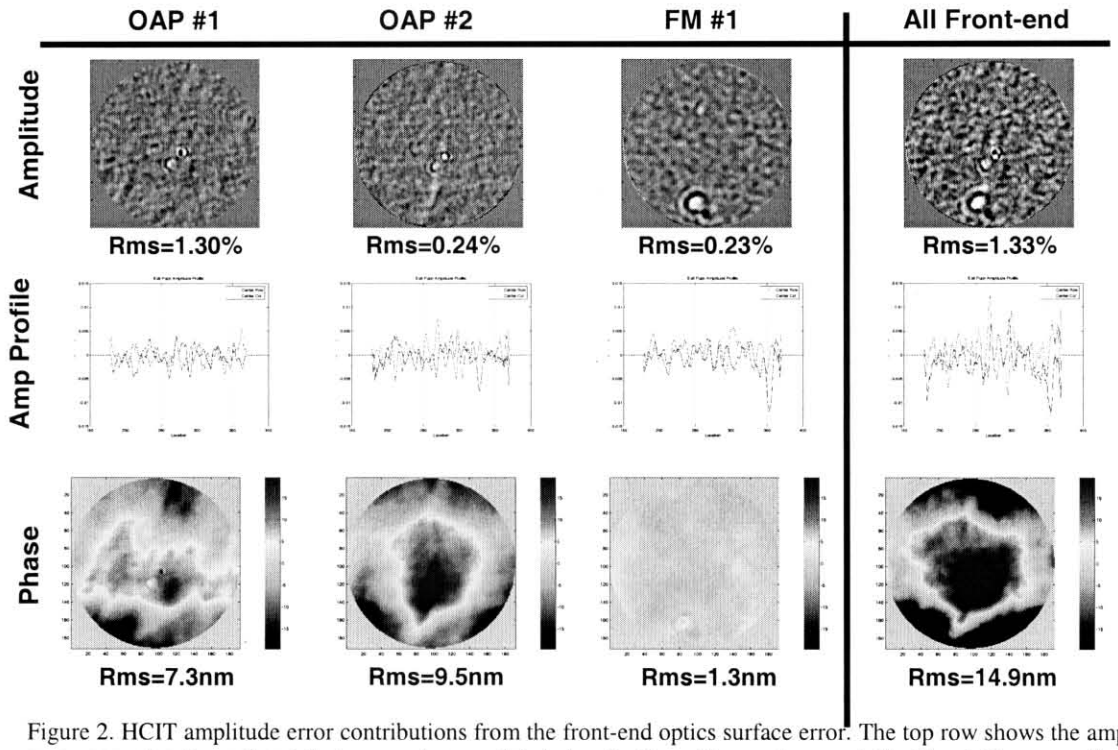

Figure 2. HCIT amplitude error contributions from the front-end optics surface error. The top row shows the amplitude error maps at exit pupil and their rms values are labeled under them. The center row is the X and Y cross section plots from the center of the amplitude map. The bottom row is the phase error of optics as measured by Zygo. First three columns show the contributions from each individual optics while the last column shows all three mirrors combined.

generate only the phase error in the wavefront. From the figure 2 we can see that the other three mirrors in the front-end optics have different amplitude error contributions. The OAP #1 has most contribution (1.3%) although it has less rms phase error than OAP #2. Detailed study has shown that the strength of phase-amplitude mixing also depends on the spatial frequency of the phase error and comparing the mirror surface PSD has shown that OAP #1 contains more high frequency error while the OAP #2 surface is dominated by the focus as shown in the figure.

To systematically study the amplitude error caused by the phase error a sinusoidal surface error with different spatial frequency is applied to each of the front-end mirrors in the model. The resulted amplitude error map at exit pupil is

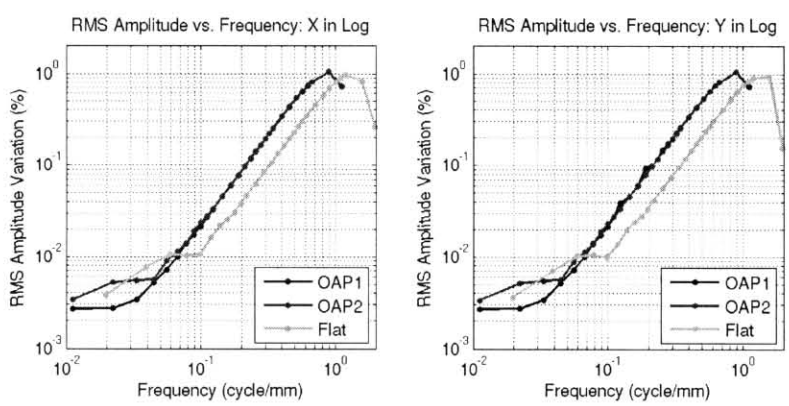

Figure 3. Modeling results of rms amplitude error vs. mirror surface error spatial frequency. The drop of curve at the high frequency end is an artifact due to the sampling limit of phase map applied to the mirror surface. For OAP #1 and #2 the diffraction propagation Fresnel number is about $F_n \approx 100$ and $F_n \approx 50$ for the Flat. The plots on the left are from sinusoidal phase in X direction and plots on the right in Y.

sinusoidal very much like the phase map and it strength is proportional to the strength of sinusoidal phase error. We calculated the rms amplitude error at each spatial frequency and we have done this for all three front end optics (again ignoring the DM since it is at the pupil) each with two sinusoidal orientations (X and Y). The plot in Figure 3 shows the amplitude error response to the spatial frequency of the mirror surface error. In the modeling a constant 1.0 micron sinusoidal is apply for all the frequency. From the plot we can see that rms amplitude error responds to the phase spatial frequency at a power law of +2. The results also show that strength of the amplitude response depends on the diffraction propagation distance from the optics to the system pupil, which can be quantified as Fresnel number F_n. Further more both orientations of the sinusoidal surface error have the similar response.

4. HCIT EXPERIMENT

Experimental measurement of amplitude error on HCIT will not only validate the modeling results but also understand and estimate the amplitude contributions from other non-phase mixing contributions such as coating uniformity and mirror cleanness. In order to reliably measure the amplitude error on HCIT we have tried several different methods. Each method has its merit and limitation. In following sections we will present and compare results of different measurement.

4.1. Measure HCIT amplitude error using pupil imaging lens

The easiest way to measure the amplitude error is to use the HCIT's built-in pupil lens to form the pupil image on the science camera. From the intensity variations of the pupil images we can get the 2D amplitude error. Figure 4 shows some sample pupil images under various pinhole sizes and source wavelength bandwidths. From these pupil images we can see that pupil intensity contains three types of the variations: the low order droop, the structural bands shown in the images when coherence source (laser) is used, and the high order variations. Table 1 summarizes the rms of amplitude errors.

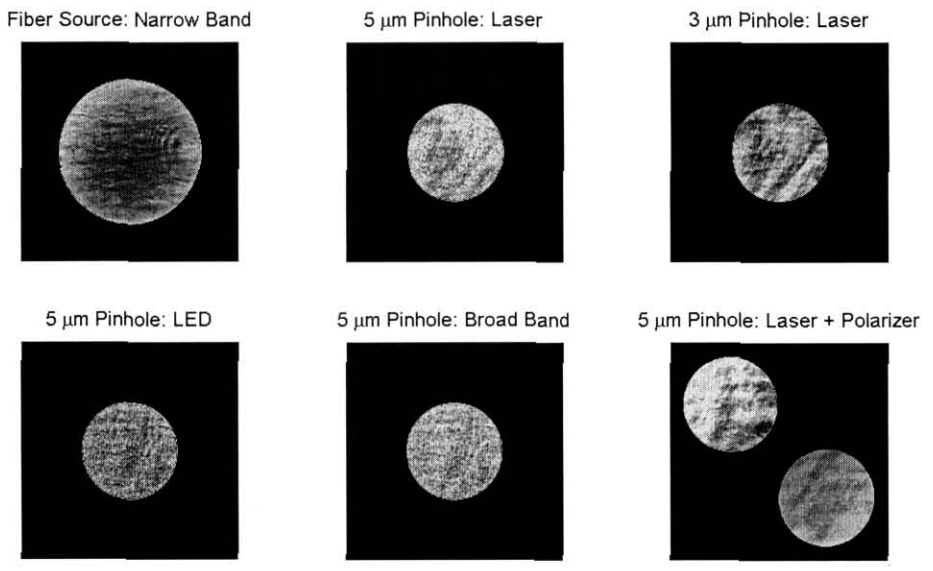

Figure 4. Sample pupil image form by HCIT's pupil lens. The source type and wavelength bandwidth is label on top of each image. The last image formed by the displacement polarizer shows pupil images at two polarization state.

The low order intensity variation of the pupil image comes mainly from the illumination pattern of the artificial star source. While the intensity map slope indicates the testbed's source module pointing mis-alignment the intensity drooping is mainly determined by the type of source. Figure 5 compares the Zernike focus term of various pupil images. It is obvious using a single mode fiber tip as the artificial star creates a much larger droop in the illumination than that

from a small pinhole. Also noticed is that as the source coherence drops the drooping flattens. This is because under incoherent light some intermediate frequency structures have disappeared which affected the low order Zernike fits.

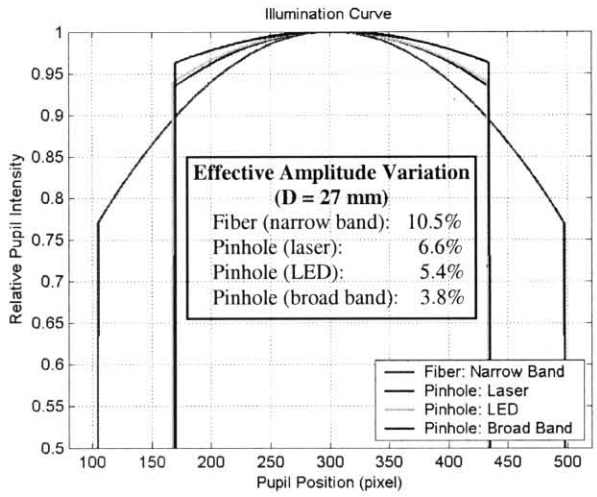

Figure 5. Comparison of amplitude drooping across the pupil from the low order Zernike fit of the pupil images. The correspondent intensity variation across the D = 27 mm diameter pupil of each curve is label in the text box.

The pupil images in Figure 4 show that some of the features in the pupil images depend on the source coherence. A separated experiment is conducted to investigate this effect. In this experiment the source diode laser driving current is varied so that the laser diode behavior changes from a laser (coherent source) to a LED (incoherent source with bandwidth of 20 nm). RMS amplitude variation is calculated on the pupil images taken with different laser diode driving current and plotted in Figure 6. The plot shows that the rms amplitude error increases as the source coherence increase, which is indicated by the increase of driving current. The effect of source coherence is apparent from the pupil images next to the plot in Figure 6. Investigation has shown that most of the intermediate frequency structures ("bands")

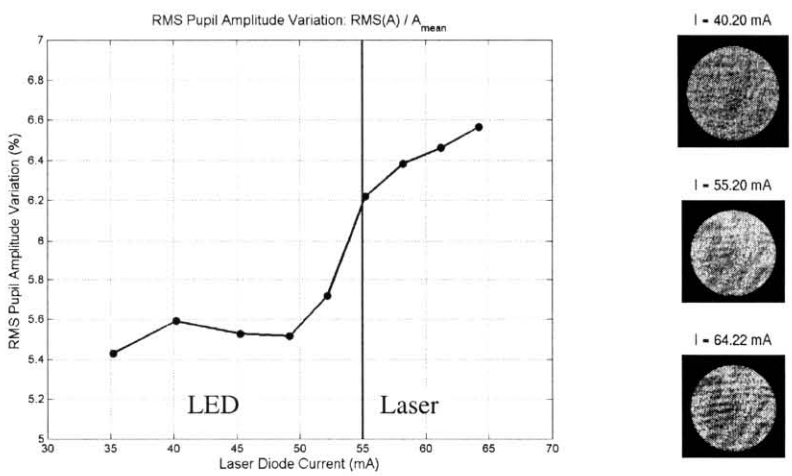

Figure 6. Effect of source coherence on amplitude error. The plot on the left shows the rms amplitude error vs. laser diode driving current which indicates source coherence. The red line indicates the lasing threshold current. The three pupil images on the right correspond to source as a LED, a laser at threshold and a laser.

seen in the coherence source pupil images are the result of interference of ghost images from camera windows and pupil lens. When source coherence decreases the interference disappears therefore lowers the rms amplitude error. The effect of pupil lens ghost has been further verified by observing the structure moves within the pupil when the pupil lens is

translated. The results from the pupil lens experiment have shown that the measurements are contaminated by the interference of ghosts from camera windows and pupil lens. The experiment measures larger rms amplitude errors for measurements taken with coherent source.

4.2. Direct pupil imagining at HCIT Lyot plane

The problems in the pupil lens imaging approach have prompted us to try to measure the pupil intensity directly by placing an imaging camera at the pupil in Lyot plane. The Lyot plane is conjugated to the HCIT pupil and is directly accessible on the testbed. An Apogee Ultra 1K x 1K CCD camera is positioned so that the CCD chip is at the Lyot plane. In this setup the pupil image is directly detected by the CCD without any imaging optics. The limited size of CCD chip causes the camera to image only partial pupil but with the translation stages the whole pupil can be mapped. However, the window of the CCD camera (needed because the chip is TEC cooled) still causes ghost and interference in the pupil image. Again, when source wavelength bandwidth increases the high contrast fringes disappears, as shown in Figure 7.

As in the case of pupil lens imaging the result of amplitude error measurements using direct pupil imaging are contaminated with interference of ghost image from camera window. The challenge of forming a clean pupil image is especially difficult because the pupil image is large in size and formed in a collimated space. Unlike the ghosts in regular point image which is formed in a focused spot the ghost images of pupil are almost always on top of the pupil image and generate interference pattern. Although the broadband pupil image avoids the coherent interference and can provide some information on the amplitude error, measuring the pupil amplitude in a narrow band source is still preferred because the features from phase-amplitude mixing is wavelength dependent and will be smeared out under the broad source.

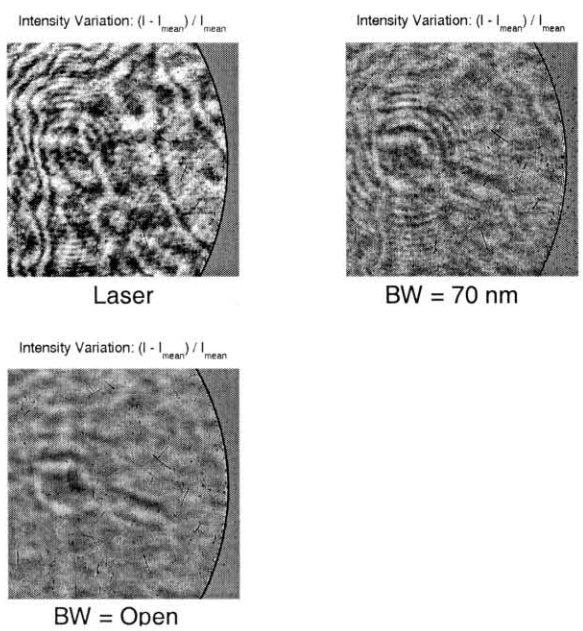

Figure 7. Direct pupil imaging under different light source wavelength bandwidths. The source wavelength bandwidth is labeled below each picture. Limited CCD size cause the camera to image only part of 27 mm pupil with edge of the pupil shown on the right.

4.3. Measure HCIT pupil intensity by fiber scanning at the Lyot plane

In order to measure the pupil image intensity without any interference from the pupil imaging system we built a 2D fiber scanning mechanism which consists of two multimode fibers, two cross mounted linear stages and a dual channel high precision power meter. The intent is to use one of the two fibers to directly sample and collect light at the Lyot plane and use the power meter to measure the intensity at the other end of the fiber. The multimode fibers have core size

of 100 micron which can provide about 300 independent samples over the 30 mm pupil. This fiber is mounted on the translation stages which can scan the Lyot plane in a programmable two-dimensional fashion. To speed up the data taking process the power meter measurements, sampled at 25 Hz, are constantly read out to a computer while the scanning stage linearly moves the fiber across the pupil. The scanning speed is kept at constant with speed slow enough for fiber to properly sample the pupil. Often times we purposely slow the scanning speed to over sample in the pupil. The scanning range of the stage is set so that the fiber samples both lit area within pupil and non-lit area beyond the pupil edge. The latter part of measurements is used as the dark background. While the scanning stages moves back and forth the other axis stage moves in steps at end of each scan so that the resulted raster motion of stages enable the fiber to sample the entire two-dimensional pupil. The second multi-mode fiber is placed at the HCIT's beam dump (Figure 1) to monitor the source intensity fluctuations. The output of this fiber is measured by the second channel of the power meter and is recorded simultaneously with pupil sample data. The source intensity monitor data is used to normalize the pupil intensity measurement. The post data process reassembles the back-and-forth raster scan data into a 2D pupil intensity map using the time stamp information recorded together with the data. Since the pupil sample happens continuously during the motion of scanning the scanning axis has much higher spatial resolution in the measurement. The program can choose either X or Y axis as the scanning axis so high resolution measurement can be made on either axes. The source used for the fiber scanning measurement is a monochromatic light from a diode laser with wavelength of 660 nm with intensity stable at ~1% level.

To estimate the measurement accuracy of the fiber scanning method we repeated scan one axis back and forth 4 times at slow speed (0.1 mm/sec). Figure 8 plots all 8 traces of measurement after the signal is normalized with source intensity and mean dark is subtracted. Since the 8 traces measures the same features of pupil the scattering of 8 measurements at each point will provide the insight of measurement error. With the mean pupil intensity at 90 pW the mean RMS scatter of the 8 measurements (not pupil amplitude errors) is 0.73 pW in the lit part of pupil, or 0.8% in intensity which is equivalent to measurement scatter of 0.4% in amplitude, The measurement scatter is 0.52 pW in the dark part of pupil (0.6% in intensity and 0.3% in amplitude). The zoom in plot in Figure 8 shows in detail the measurement scatter as well the pupil amplitude variation features. The rms stage position error, which is calculated by the scatter of rising and falling edged of pupil intensity, is about 0.02 mm over the 30 mm pupil, well within the size of fiber core (0.1 mm). The statistics as well as the superposed plot of repeated traces have shown that the scanning fiber measurement can reliably measure the pupil amplitude error features which is as strong as 1.3% (~2.6% in intensity) predicted by the modeling.

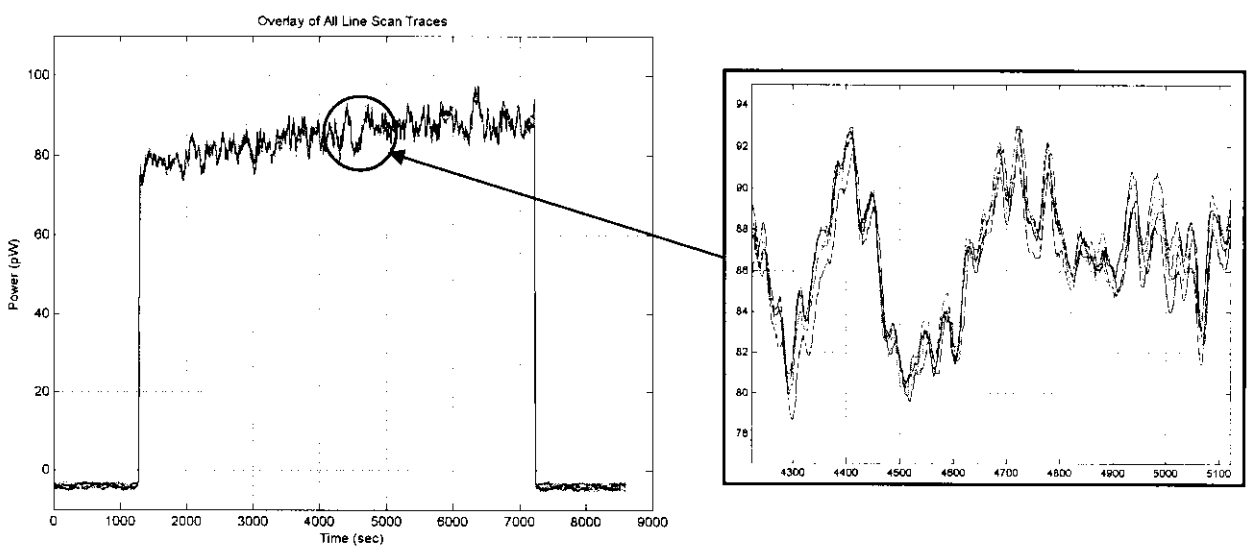

Figure 8. Repeated line scanning measurements of pupil at HCIT's Lyot plane. The plot shows 8 scanning traces. The zoom-in plot on the right shows the measurement scatter as well as the intensity variation associated with pupil amplitude error.

Figure 9 shows the pupil intensity map combined from intensity maps with scanning axis of X and Y (Figure 9 left). The major contribution of the intensity variation is the slope and drooping from the source illumination (Figure 9 middle). Although the measurement along the scanning axis is continuous the measurement along stepping axis, a step

size of 0.7 mm in this map, is discrete and values are interpolated in the intensity map. That is why the pupil intensity map shown in Figure 9 contains some squarish blocks which are corresponding to 0.7 x 0.7 mm area. Amplitude errors calculated from both the repeated line scan and 2D intensity map are summarized in Table 1.

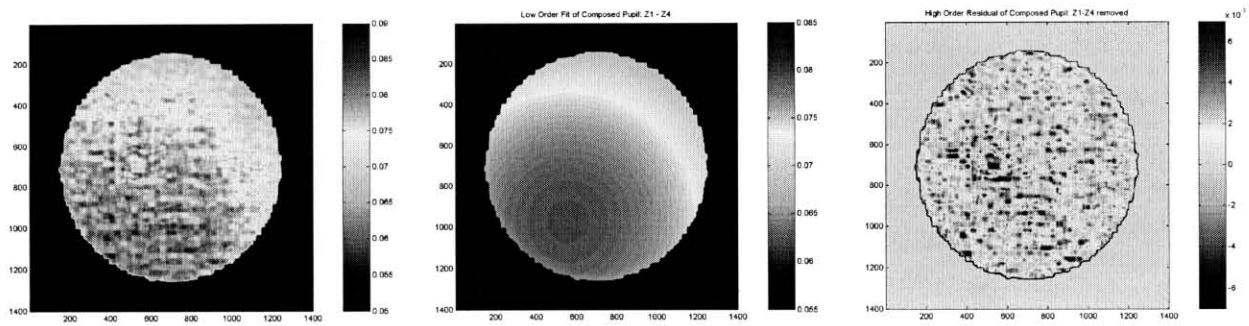

Figure 9. *Left*: Composite 2D intensity map of pupil measured by fiber scanning at HCIT Lyot plane. *Middle*: Fitted low order intensity variations dominant by the source illumination pattern (drooping) and pointing mis-alignment (tilts). *Right*: High order intensity variations after the low order pattern removed. Color bar on the right shows the intensity scale in unit of nW.

Table 1 summarizes the experimental measurement of amplitude errors on HCIT. The measurements have shown that under monochromatic light the pupil imaging with pupil lens or direct imaging with camera all have larger amplitude errors. By comparison the pupil lens measurement is worse than that of direct imaging since there are more optical components to generate ghost images. Opening up wavelength bandwidth helps lower the amplitude errors but the results are not desirable for understanding the phase mixing. Without interference from any optics the fiber scanning measurement resulted in the smallest amplitude error of all methods.

Table 1. Summary of the experimental measurements of amplitude error on HCIT. For each measurement listed the measured intensity variations are converted into amplitude errors. Rms amplitude errors are calculated on original amplitude map (*"All Image" column*), low order fit amplitude map (*"Low Order" column*), and residual high order amplitude map with low order map removed (*"High Order" column*),

Measurement	**Fiber Scanning: Composed 2D**			**Fiber Scanning: Mean Repeated Lines**		
Order	All Image	Low Order	High Order	All Image	Low Order	High Order
RMS Ampl.	2.83%	2.03%	1.94%	2.44%	2.01%	1.38%
Measurement	**Pupil Lens Imaging: Laser**			**Pupil Lens Imaging: LED (20 nm)**		
Order	All Image	Low Order	High Order	All Image	Low Order	High Order
RMS Ampl.	6.57%	1.71%	6.34%	5.43%	1.24%	5.29%
Measurement	**Direct Pupil Imaging: Laser**			**Direct Pupil Imaging: Broadbad**		
Order	All Image	Low Order	High Order	All Image	Low Order	High Order
RMS Ampl.	3.55%	0.46%	3.52%	1.60%	0.47%	1.53%

5. SUMMARY

As a critical part of wavefront sensing and control understanding and quantitatively measuring wavefront amplitude error is of great importance to HCIT. Both modeling and experimental approaches have been used to address this issue.

Using a realistic as-built optical model and measured mirror surface information we calculated the amplitude error caused by the phase-amplitude mixing to be about *1.3%* for the current $\lambda/20$ optics used in HCIT. Understandably the strength of phase-amplitude mixing depends on the diffraction propagation distance to the system pupil. However, our modeling study has also shown that the phase mixed amplitude responses to the phase error at a power law of *+2* to the

phase spatial frequency. With greater mixing effect on higher frequency surface error this effect may place a stricter requirement on the mirrors.

Approaches to experimentally measure the amplitude error on HCIT turned out to be nontrivial. The experiments results were contaminated by the interference from the ghost reflections in pupil imaging system. Eventually we came up with the method of two-dimensional fiber scanning at Lyot plane, a slow brute force method which directly measures the intensity of pupil at Lyot. Although less efficient than other two pupil imaging methods the fiber scanning approach proves to be reliable for amplitude error measurement with its small measurement scatter and high position accuracy.

The average experimental measurements from fiber scanning method have put the testbed amplitude error at ~2.6% with a major contribution from the testbed source illumination (~2.0%). With the illumination contribution (low order) removed the amplitude error is about ~1.6%. This value is still larger than what model has predicted (~1.3%). However, the optical model only considered the amplitude error caused by mixing from mirror surface error. Other factors such as optical coating and mirror surface cleanness will also contribute to the amplitude error.

This paper describes our initial efforts to understand the amplitude error on HCIT. The study is still continuing, both in modeling and experimentation. The HCIT model will be updated to add the near field diffraction propagation on the back-end optics. More fiber scanning measurements will be carried in finer steps for better pupil sampling. Also, measurements will be made at different wavelengths with the hope to differentiate amplitude error caused by phase mixing, which is wavelength dependent, from mirror coating uniformity and surface cleanness. Although pupil imaging results are contaminated by the ghost interference we can still take the advantage of its high efficiency to monitor the testbed illumination changes by image differentiation. Our ultimate goal, set by the TPF project, is to valid the HCIT model with the HCIT measurement.

ACKNOWLEDGEMENTS

This research was carried out at the Jet Propulsion Laboratory, California Institute of Technology, under a contract with the National Aeronautics and Space Administration (NASA).

REFERENCES

[1] Terrestrial Planet Finder web site, http://tpf.jpl.nasa.gov

[2] R. P. Linfield, "Wavefront amplitude errors for a TPF Coronagraph: their effects and possible correction," in *Optical, Infrared, and Millimeter Space Telescopes*, John C. Mather, editor, Proc. SPIE **5487**, 1255-1263 (2004).

[3] A. E. Lowman, J. T. Trauger, B. Gordon, J. J. Green, D. Moody, A. F. Niessner, and F. Shi, "High Contrast Imaging Testbed for the Terrestrial Planet Finder Coronagraph," in *Optical, Infrared, and Millimeter Space Telescopes*, John C. Mather, editor, Proc. SPIE **5487**, 1246-1254 (2004).

[4] J. T. Trauger, C. Burrows, B. Gordon, J. J. Green, A. E. Lowman, D. Moody, A. F. Niessner, F. Shi, and D. Wilson, "Coronagraph contrast demonstrations with the High Contrast Imaging Testbed," in *Optical, Infrared, and Millimeter Space Telescopes*, John C. Mather, editor, Proc. SPIE **5487**, 1330-1336 (2004).

[5] N. J. Kasdin, R. J. Vanderbei, M. G. Littman, M. Carr, and D. N. Spergel, "The shaped pupil coronagraph for planet finding coronagraph: optimization, sensitivity, and Laboratory testing," in in *Optical, Infrared, and Millimeter Space Telescopes*, John C. Mather, editor, Proc. SPIE **5487**, 1312-1321 (2004).

[6] D. C. Redding and W. Breckenridge, "Optical modeling for dynamics and control analysis," *Journal of Guidance, Control, and Dynamics*, Vol. **14**, No. 5, Sept. - Oct. (1991).